Sustainable Carbon Materials

Original Research

Open Access

https://doi.org/10.48130/scm-0025-0004

CO_2 capture performances of H_3PO_4/KOH activated microwave pyrolyzed porous biochar

Tianhao Qiu[1], Weitao Cao[1], Kaihan Xie[1], Faizan Ahmad[1], Wenke Zhao[1], Ehab Mostafa[2] and Yaning Zhang[1*]

Received: 30 June 2025

Revised: 1 August 2025

Accepted: 22 September 2025

Published online: 27 October 2025

Abstract

As global climate change intensifies, carbon dioxide emissions have become a significant threat to ecological security and sustainable development. This study introduces a novel microwave-assisted two-step activation strategy (preliminary H_3PO_4 activation and KOH etching), to prepare hierarchically porous biochar from corn straw with optimized CO_2 adsorption capacity. The investigation focused on the influence of the H_3PO_4-to-biomass impregnation ratio on the performance of the biochar. The results indicate that sample PKBC-3, synthesized at an impregnation ratio of 3:1, exhibits a specific surface area as high as 3,038.92 m^2/g and a micropore volume of 1.089 cm^3/g. Under conditions of 25 °C and 1 bar, PKBC-3 achieves a maximum CO_2 adsorption capacity of 3.434 mmol/g. Crucially, dynamic adsorption experiments (15% CO_2, 100 mL/min) confirm that the 42.4% proportion of mesopore volume significantly enhances adsorption kinetics, resulting in a dynamic adsorption capacity of 3.02 mmol/g. Furthermore, the findings reveal that a low mesopore proportion (< 30%) can moderately retain adsorption capacity while restricting kinetics. Conversely, an excessive mesopore proportion (> 50%) may lead to micropore collapse, thereby reducing adsorption capacity. This research provides valuable insights for the design of biomass-derived adsorbents, aiming to achieve an optimal balance between high capacity and rapid kinetics through precise control of mesopore proportions.

Keywords: CO_2 adsorption, Porous biochar, Microwave pyrolysis, H_3PO_4/KOH activation, Corn straw

Highlights

- Corn straw-based biochar was produced by microwave pyrolysis and two-step activation.
- Isotherms, breakthrough curves, and kinetic curves were presented for CO_2 adsorption.
- The maximum specific surface area was 3,030 m^2/g at H_3PO_4/biomass mass ratio of 3:1.
- The maximum CO_2 adsorption capacity was 3.434 mmol/g at 25 °C and 15 mL/min.

* Correspondence: Yaning Zhang (ynzhang@hit.edu.cn)

Full list of author information is available at the end of the article.

Graphical abstract

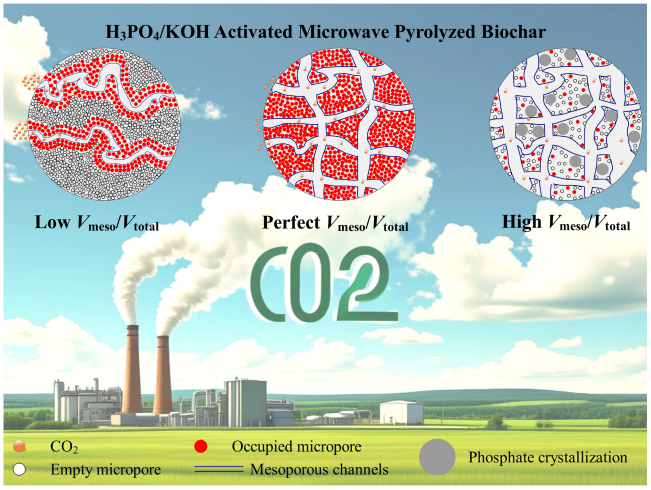

Introduction

Greenhouse gas emissions, primarily CO_2, pose significant risks to ecological security and sustainable development[1–4]. As of 2024, global anthropogenic CO_2 emissions have reached 41.6 billion metric tons, with atmospheric concentration at 422.5 ppm, representing a 52% increase compared to pre-industrial levels. Addressing ensuing crises, including global warming, necessitates the implementation of carbon capture, utilization, and storage. Among these technologies, post-combustion capture technology is increasingly regarded as one of the most promising directions, given its potential for direct integration with existing industrial flue gas treatment systems and its relatively low technical risk. Industrial flue gases typically comprise 12%–15% CO_2, along with N_2, NO_x, and SO_x. While traditional amine scrubbing has been successfully commercialized, it faces several bottlenecks, including high energy consumption, solvent degradation toxicity, and severe equipment corrosion[5]. In contrast, solid adsorption technology has gained considerable attention due to its operational flexibility, potential for lower energy consumption, and favorable economic characteristics[6]. Particularly, carbonaceous adsorbents (e.g., activated carbon, carbon nanotubes, biochar) have emerged as important alternatives due to their excellent stability, hydrophobicity, and cost-effectiveness[7]. Biochar, a porous carbon, is produced from thermochemically converted biomass waste, delivering both environmental and economic benefits[8]. Its production process is carbon-negative, sequestering ~50% biomass carbon while mitigating emissions associated with open burning[9]. Moreover, biochar makes use of low-cost, abundant feedstocks and has tunable porosity/surface chemistry for enhancing its adsorption capabilities[10]. Importantly, saturated biochar can serve as a long-term carbon sink, whether through soil amendment (enhancing ecological sequestration) or as construction materials[11–13]. This integrated approach to carbon capture, sequestration, and utilization positions biochar as a sustainable and cost-effective solution for the bottlenecks of industrial carbon capture.

Currently, pyrolysis technology for biochar preparation serves as a vital component in carbon sequestration and pollution control mitigation, significantly influencing the material's pore structure, surface chemistry, and ultimate application performance. Conventional pyrolysis methods, including slow pyrolysis and fast pyrolysis, facilitate the thermochemical conversion of biomass by regulating heating rates (5–30 °C/min), residence times (> 30 min), and inert atmospheres (such as N_2 and CO_2), resulting in the formation of carbon materials enriched with functional groups, including carboxyl and carbonyl, through a series of multi-stage reactions of dehydration, depolymerization, and carbonization[14,15]. However, these methods present drawbacks, including uneven heating, high energy consumption, and limited pore development[16]. In contrast, microwave-assisted pyrolysis generates volumetric heating effects through interactions between electromagnetic fields and biomass dipole molecules (e.g., water, polar groups in lignin), thereby improving energy transfer efficiency by 3 to 5 times compared to conventional conductive heating and completing carbonization within 15 min[17]. This unique heating mechanism originates from microwave-selective excitation of dielectric loss in materials. When the frequency of the electromagnetic waves aligns with the molecular dipole relaxation frequency, polar molecules undergo rapid rotational friction, generating heat that instantly creates localized high-temperature hotspots within the biomass. This triggers rapid pyrolysis reactions, leading to the formation of interconnected mesopore and macropore networks[18]. Figure 1 shows the mechanisms of microwave-assisted pyrolysis and conventional pyrolysis[19,20]. Experiments demonstrate that rice straw-derived biochar via microwave pyrolysis attains a specific surface area of 455.90 m^2/g, representing a 58% increase over conventional methods (288.60 m^2/g), with a more uniform pore size distribution and an enhanced CO_2 adsorption capacity (80 mg/g)[21]. Additionally, microwave-induced interfacial polarization enhances interactions between metal activators and biomass components. In a related study, Lin et al.[17] prepared hydrophobic biochar via microwave-ferric chloride co-activation, yielding a benzene-series adsorption capacity of 136.60 mg/g with a 40% increase in surface oxygen-functional group density when compared to conventional pyrolysis products.

Despite the significant pore development achieved through microwave pyrolysis, the pore structure and adsorption performance of biochar remain notable discrepancies when compared to conventional activated carbon. To address this limitation, activation techniques aimed at directional modulation of biochar pore networks through physical or chemical means have become crucial strategies. Physical methods, such as CO_2 or steam activation, selectively etch carbon, leading to a significant increase in surface area

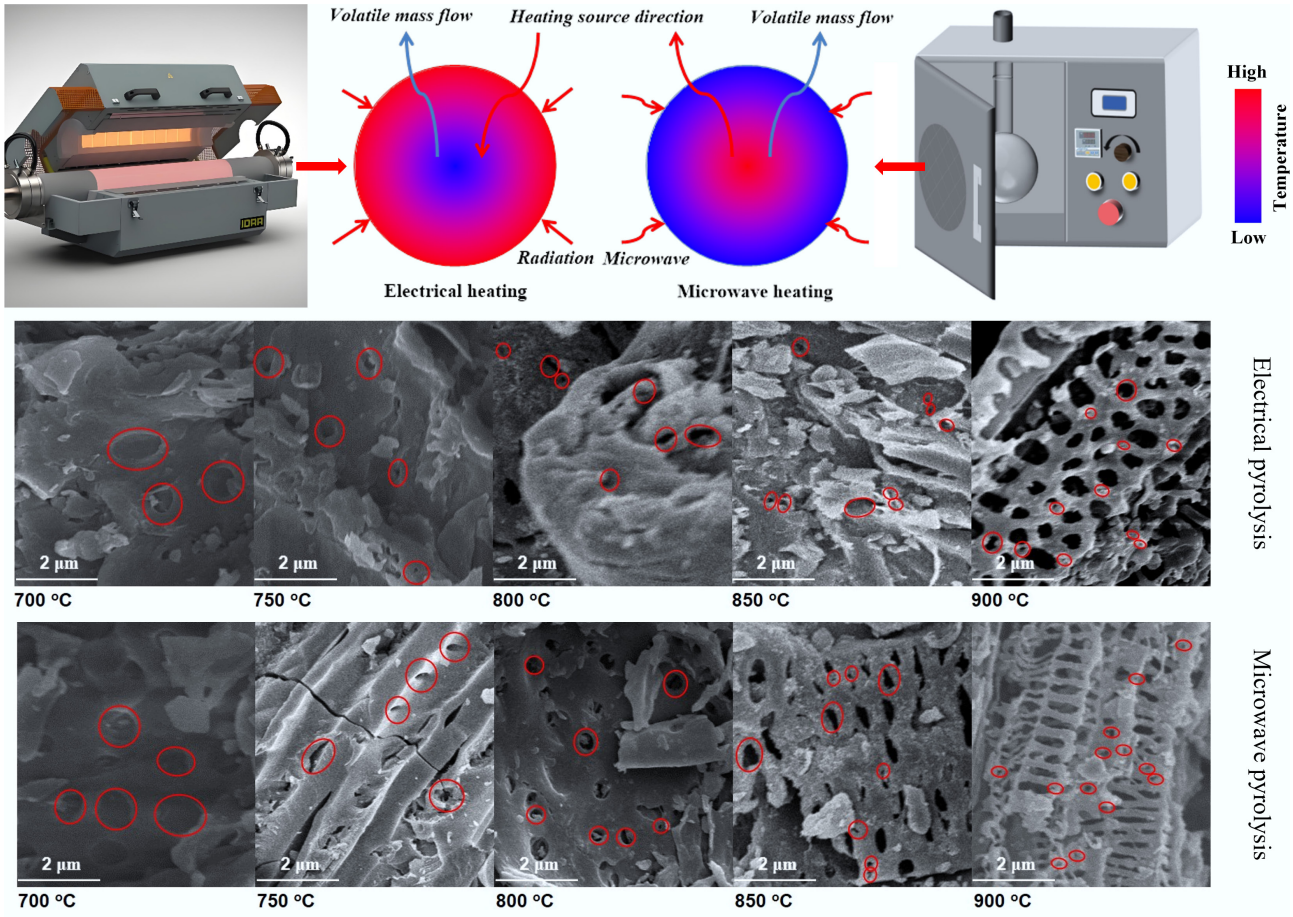

Fig. 1 Diagram of comparison between microwave pyrolysis and conventional pyrolysis[19,20].

and pore volume[22]. Additionally, steam activation promotes the formation of uniform micropores and retains functional groups[23]. In contrast, chemical activation allows for finer control of pore structures through the intercalation-expansion-etching mechanism between activating agents and biomass. KOH activation is dominant for creating ultra-microporous biochar (< 1 nm, > 80% micropores) with a remarkably high specific surface area (> 3,000 m^2/g). This process occurs in several stages: molten KOH infiltration (< 400 °C), intercalation-expansion (400–700 °C), and vapor-phase etching (> 700 °C)[24,25]. For example, Xie et al.[26] prepared soybean residue-based biochar using this method, achieving a micropore ratio of 91% and a CO_2 adsorption capacity of 6.3 mmol/g (1 atm). However, excessive reliance on micropores can limit adsorption kinetics. Mestre et al.[27] noted that materials with high surface area but deficient mesopores often exhibit slow kinetic characteristics during practical adsorption, leading to significantly reduced adsorption rates. In addressing this issue, phosphoric acid activation presents distinct advantages. Its acidic environment preferentially dissolves ash, metal oxides, and organic impurities, thereby eliminating pore blockages while generating 2–50 nm mesoporous channels. And this process results in the construction of a more developed three-dimensional pore network, which is critical for efficient mass transfer[28]. Concurrently, the dehydrating action of the acid activator promotes carbon skeleton cross-linking and aromatization, forming a stable mesoporous framework. Zhang et al.[29] employed CH_3COOK to activate sludge-derived biochar after metal impurities were removed by HCl pretreatment, achieving a specific surface area of 991.55 m^2/g. And this process led to a 70% increase in Pb^{2+} adsorption capacity, confirming the critical role of open pores in heavy metal diffusion. Microwave technology further optimizes activation by allowing for deep KOH penetration into biomass and accelerating intercalation reactions, which significantly reduces activation time (e.g., 10 min vs 2 h)[30,31]. Selective heating also helps maintain the integrity of the pore structure. Corn straw presents an ideal biomass for this approach due to its abundant agricultural waste rich in lignocellulose, making it highly suitable for thermochemical conversion. Additionally, its inherent silica and mineral content necessitate effective activation strategies, such as H_3PO_4 treatment, to remove impurities while concurrently developing mesopores.

Based on the above, this study employs a modified two-step activation method. First, biomass is impregnated and washed with phosphoric acid (10%–30%), followed by low-to-mid-temperature activation to achieve directional mesopore construction via acid concentration modulation. Next, the pretreated biochar undergoes microwave-KOH activation, which takes advantage of alkali metal gasification-expansion to refine the micropore network. The characterization of the material's pore size distribution and morphology was conducted through N_2 adsorption/desorption and scanning electron microscope (SEM). Particular emphasis was placed on analyzing the impact of phosphoric acid impregnation ratios on the mesopore proportion. Subsequently, the CO_2 adsorption characteristics of the prepared biochar were investigated. The integration of adsorption models with kinetic models allowed for an evaluation

of the enhancement in mass transfer efficiency provided by hierarchical pore channels. This study provides both theoretical foundations and practical strategies for developing CO_2 adsorbents with high adsorption capacity and rapid kinetics.

Materials and methods

Materials

Corn straw was sourced from Jiangsu Province, China. First, the straw was washed with deionized water and then dried at 60 ℃ for 24 h. Subsequently, the dried straw was ground and sieved through a 60-mesh sieve (particle size < 250 μm) and then stored in an airtight container at room temperature prior to experiments. The proximate and ultimate analyses of the straw are detailed in Table 1. The data for proximate analysis were determined according to the Chinese National Standard GB/T (Tuijianxing Guojia Biaozhun, Recommended National Standard) 212-2008, while the ultimate analysis data followed the Chinese National Standard GB/T 31391-2015.

During microwave-assisted pyrolysis, microwave energy exhibits selectivity toward raw materials. Given the inadequate microwave absorption of corn straw, the incorporation of microwave absorbers is required. These absorbers function by absorbing microwave radiation, converting it into other forms of kinetic energy that are further dissipated as thermal energy. This process enhances heating efficiency and facilitates the microwave-assisted pyrolysis reaction. For this study, silicon carbide (SiC) was selected as the microwave absorber. SiC possesses a density of 3,230 kg/m^3 and a particle size of ~2 mm. Electronic-grade KOH crystals and an 85 wt.% H_3PO_4 solution was purchased from Shanghai Macklin Biochemical Technology Co., Ltd. (Shanghai, China). Furthermore, high-purity (99%) N_2 and CO_2 gases were obtained from Beijing Hai Pu Gas Co., Ltd. (Beijing, China).

Experimental procedures

The experimental setup for microwave-assisted pyrolysis and activation of biomass is illustrated in Fig. 2. This system comprises four components: (a) vacuum pump system (5, 6), (b) temperature measurement system (3, 4), (c) heating system (1, 2), and (d) power measurement system (7). The microwave pyrolysis apparatus has been manufactured by Shanghai Longyu Microwave Equipment Co., Ltd. (Shanghai, China) with a rated power of 1,000 W and a frequency of 2,450 MHz.

During the pyrolysis, the reaction temperature was monitored in real time using K-type thermocouples, with readings displayed on a temperature reader. The specific procedure for microwave pyrolysis experiments is detailed below. First, the microwave absorber and pyrolysis feedstock were mixed in the quartz reactor. Subsequently, the pyrolysis experimental system was connected as shown in Fig. 2. After connecting all test pipelines, quartz wool was used to insulate the quartz reactor inside the microwave furnace. The valve was opened to introduce N_2 gas at a flow rate of 0.2 L/min. After 20 min, the microwave furnace was activated to initiate the microwave pyrolysis reaction. The experimental procedure for the two-step activation of biomass is depicted in Fig. 3. This procedure comprises two steps: H_3PO_4 impregnation with preliminary microwave activation, and KOH impregnation combined with high-temperature microwave activation. All activation parameters (temperatures, times, KOH/biochar ratio) were optimized through pre-experiments and fixed at their optimal values. The H_3PO_4/biomass ratio was designated as the primary variable. Specific experimental details are provided as follows.

H_3PO_4 impregnation and preliminary microwave activation: 15 g of pretreated biomass was mixed with a 40 wt.% H_3PO_4 solution at specified impregnation ratios (1:1, 1:2, 1:3, 1:4) to ensure complete saturation. The mixture was stirred and impregnated for 24 h at room temperature with a magnetic stirrer. Subsequently, the impregnated mixture was transferred to a quartz reactor for microwave-assisted pyrolysis. Since H_3PO_4 activation effectively generates mesopores at lower temperatures, insufficient activation (< 400 °C) yields fewer mesopores, while excessive temperatures (> 550 °C) can cause mesopore collapse, resulting in the formation of macropores and a reduced yield. Therefore, the activation temperature was set to 450 °C for a pyrolysis duration of 30 min. The resulting phosphoric acid-activated biochar (PBC) was washed with deionized water multiple times until the eluate reached neutrality, ensuring the complete removal of residual H_3PO_4 and soluble phosphates. The washed PBC was dried at 105 °C for 24 h.

KOH impregnation and high-temperature microwave activation: KOH solution and PBC were mixed uniformly at a KOH mass ratio of 3:1. The mixture was stirred for 24 h at room temperature using a magnetic stirrer. Subsequently, the impregnated mixture was transferred to the quartz reactor for microwave-assisted pyrolysis. As KOH activation requires higher temperatures for effective micropore etching, the pyrolysis temperature was set to 750 °C for 60 min. The resulting two-step activated biochar (PKBC) was thoroughly washed with deionized water until the eluate approached neutrality, ensuring the complete removal of any residual strong bases (e.g., KOH, K_2CO_3). The washed PKBC was dried at 105 °C for 24 h. To further explore the effects of the first-step H_3PO_4 activation, control experiments were conducted in which corn straw biomass was directly pyrolyzed at 450 °C without phosphoric acid activation. The activated biochar obtained via this method is denoted as KBC. The specific experimental conditions studied are summarized in Table 2.

Table 1 Proximate analysis and ultimate analysis of corn straw

Item		Value
Proximate analysis (wt.%)	Moisture	5.11
	Ash	8.66
	Volatile	71.23
	Fixed carbon	15.00
Ultimate analysis (wt.%)	C	42.24
	H	5.78
	O	37.78
	N	0.39
	S	0.04

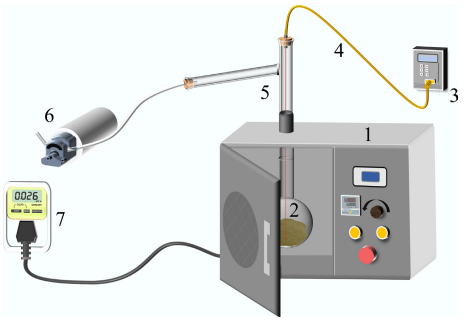

Fig. 2 Diagram of microwave-assisted pyrolysis experimental equipment: (1) microwave oven, (2) quartz reactor, (3) temperature sensor, (4) K-type thermocouple, (5) adapter connecting pipe, (6) vacuum pump, and (7) electric meter.

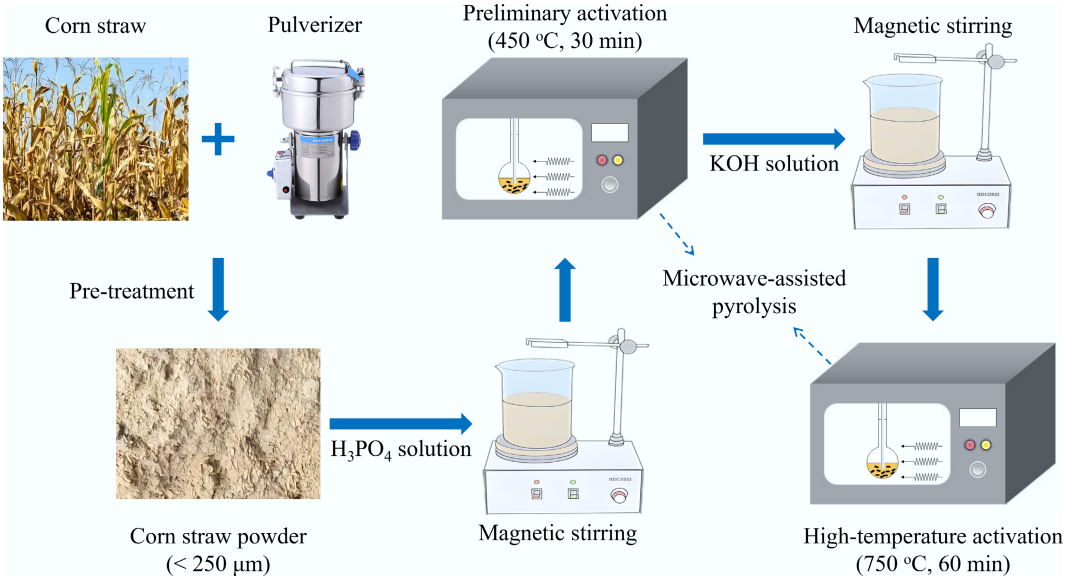

Fig. 3 Two-step activation experimental process.

Characterizations

The adsorption-desorption isotherms of biochar were measured at 77 K under a nitrogen atmosphere using a gas adsorption analyzer (Autosorb-iQ, Quantachrome Instruments, USA). Prior to testing, the samples were degassed at 200 °C for 12 h. The specific surface area of the biochar was determined using the BET (Brunauer-Emmett-Teller) method, which is based on the adsorption isotherms showing gas uptake versus relative pressure. Data regarding pore size distribution and pore volume of the biochar were analyzed using the BJH (Barrett-Joyner-Halenda) and HK (Horvath-Kawazoe) methods to calculate the average pore diameter. After being coated with gold, the surface morphology of the biochar was scanned using an SEM (JSM-7800 F Prime, JEOL). The acceleration voltage was set within a range of 0.5 to 30 kV, with a secondary electron resolution of 0.8 nm (at 15 kV acceleration voltage).

CO_2 capture experiments

The static adsorption isotherms for CO_2 within the pressure range of 0–1 bar were measured using a Micromeritics ASAP 2460 analyzer. Prior to testing, all samples were degassed under vacuum at 200 °C for 12 h to completely remove physically adsorbed water and gases. This was followed by isothermal adsorption measurements conducted at 25 °C. Subsequently, quasi-equilibrium adsorption kinetic data of biochar for CO_2 were obtained by monitoring the time-dependent variation in adsorption capacity at a pressure of 0.15 bar and different temperatures (0–45 °C), until adsorption equilibrium was reached. For dynamic adsorption characterization, a fixed-bed breakthrough experimental setup was established. The system operated at 25 °C with a gas mixture of 15% CO_2 and 85% N_2, simulating typical flue gas composition. This mixture flowed through an adsorption column packed with 1 g of activated biochar at a flow rate of 100 mL/min. The temporal variation of outlet gas concentration was continuously monitored using online gas chromatography to determine the dynamic adsorption breakthrough curves.

Table 2 Experimental conditions of biochar activation

Sample	KBC	PKBC-1	PKBC-2	PKBC-3	PKBC-4
H_3PO_4/biomass	0	1:1	2:1	3:1	4:1

Results and discussion

BET surface area and pore characteristics of biochar properties

The results from nitrogen adsorption experiments conducted at 77 K for different samples demonstrate the significant impact of the phosphoric acid impregnation ratio on the pore structure of corn straw-based biochar. Across the gradient variation from impregnation ratios of 0:1 to 4:1, the pore parameters of the materials exhibit a non-monotonic evolution characterized by initial optimization followed by attenuation, as shown in Table 3. Specifically, as the impregnation ratio increases from 0:1 for the control group KBC to 3:1 for PKBC-3, the specific surface area (SSA) experiences a stepwise increase from 1,340 to 3,040 m^2/g (representing a 127% increase). The total pore volume (V_{total}) also expands significantly, rising from 0.6 to 1.9 cm^3/g (an increase of 217%). The contribution of micropores is particularly prominent, with the micropore volume (V_{micro}) increasing from 0.5 to 1.1 cm^3/g (an increase of 120%). Besides, V_{meso} represents the mesopore volume. The nitrogen adsorption isotherms presented in Fig. 4 illustrate that all samples exhibit mixed Type I (steep rise in the

Table 3 Pore structure parameters of biochar

Sample	SSA (m^2/g)	V_{total} (cm^3/g)	V_{micro} (cm^3/g)	V_{meso} (cm^3/g)	V_{meso}/V_{total} (%)	Average pore size (nm)
KBC	1,338.74	0.614	0.512	0.102	16.61	1.64
PKBC-1	2,088.10	0.898	0.653	0.345	27.28	1.82
PKBC-2	2,993.07	1.638	1.021	0.617	37.67	1.98
PKBC-3	3,038.92	1.891	1.089	0.802	42.41	1.93
PKBC-4	1,709.26	0.699	0.319	0.380	54.42	2.11

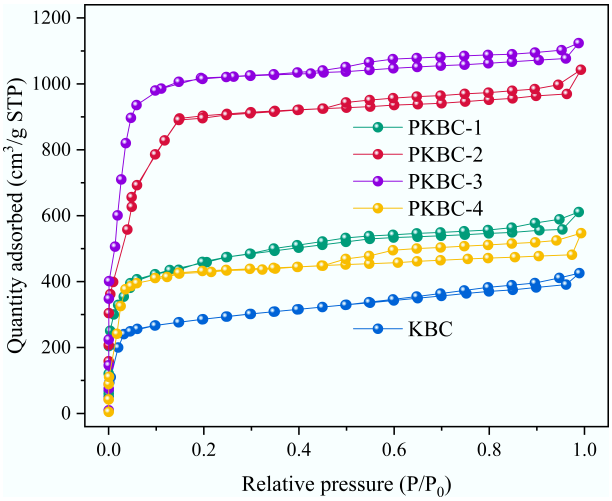

Fig. 4 Nitrogen adsorption and desorption isotherms for different samples.

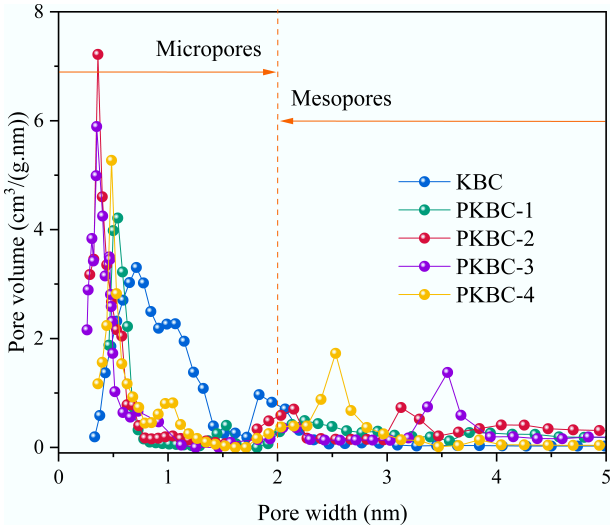

Fig. 5 Pore size distribution of different samples.

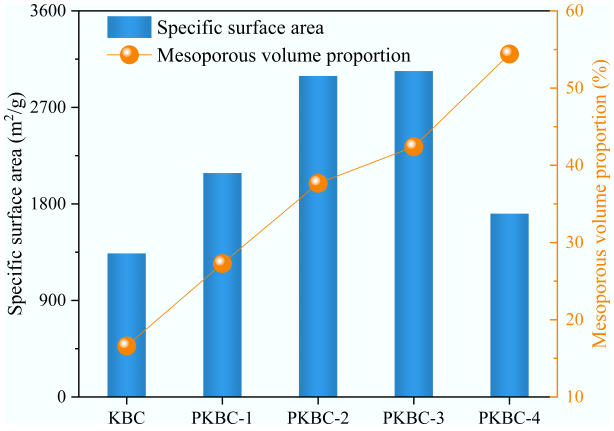

Fig. 6 Mesoporous volume proportion of different samples.

P/P_0 < 0.1 region) and Type IV (gentle slope increase in the P/P_0 > 0.4 region) characteristics, indicating the presence of both micropores and mesopores in the materials and confirming their dual capability of micropore adsorption and mesopore capillary condensation[32]. PKBC-3 displays a distinct H4-type hysteresis loop in the P/P_0 > 0.4 region, which signifies the formation of a lamellar mesoporous structure. In contrast, the hysteresis loop area of PKBC-4 drastically shrinks, suggesting pore collapse due to over-activation.

The pore size distribution curves in Fig. 5 provide further insight into the evolution mechanism of the pore structure. The KBC samples that do not undergo H_3PO_4 treatment show a wide micropore distribution centered at 0.5–1.5 nm, reflecting the inherent micropores present in natural cellulose-derived carbon activated solely by KOH. As the ratio of the H_3PO_4 increases, the peak intensity in the region below 2 nm continuously intensifies, confirming the selective etching effect of phosphoric acid on cellulose microcrystals. When the ratio of H_3PO_4/biomass is 1:1, a distinct micropore peak appears at 0.52 nm due to the partial dissolution of hemicellulose and lignin, which improves the uniformity of the pores. Increasing the ratio to 2:1 resulted in the formation of double peaks at 0.35 nm (ultrafine pores) and 3.2 nm (mesoporous pores). This change is linked to the enhanced etching of cellulose microcrystals and the initial removal of lignin, which leads to small mesoporous voids. For the 3:1 sample, the mesoporous peak shifted further to 3.5 nm while maintaining the microporous peak at 0.35 nm. This shift occurred because the higher concentration of phosphoric acid dissolved more lignin, thereby expanding the mesoporous framework. However, at a ratio of 4:1, excessive acid corrosion caused structural degradation. As a result of the thinning of the pore walls, the micropore peaks widened to 0.50 nm. Additionally, due to the partial collapse and merging of adjacent pores during the KOH activation process, the mesopore peaks contract to 2.5 nm, which is consistent with the observed decrease in micropore volume to 0.32 cm^3/g.

Figure 6 illustrates the mesopore proportions of different samples, revealing a dual-threshold pattern during the activation process. The results indicate that the mesopore proportion exceeds 30% at a phosphoric acid impregnation ratio of 1:1, indicating the initiation of hierarchical pore construction. In the range of 2:1 to 3:1 for the impregnation ratio, the mesopore proportion stabilizes near 40%, while the micropore volume remains at least 1 cm^3/g. This suggests that phosphoric acid impregnation within this range effectively promotes mesopore formation without significantly sacrificing the micropore volume[33]. However, when the impregnation ratio reaches 4:1, the mesopore proportion sharply declines to 33.3% (with an absolute value of only 0.23 cm^3/g), and there is a 52% reduction in micropore volume (down to 0.32 cm^3/g). This decline is primarily due to excessive phosphoric acid leading to over-hydrolysis of the precursor, which results in the formation of unstable oligosaccharide phosphate esters that can fracture the carbon framework during microwave pyrolysis. The loosened framework undergoes structural reorganization during KOH activation, where some micropores merge into ineffective macropores. Additionally, residual phosphates block pores, reducing the effective specific surface area.

Comprehensive characterization data indicate that the regulation of the final pore structure through the phosphoric acid impregnation ratio follows a three-step synergistic pathway. During the H_3PO_4 pre-activation stage, H_3PO_4 selectively deconstructs the lignin-hemicellulose network through esterification reactions. Within the 2:1–3:1 range, H_3PO_4 forms molecular templates between cellulose microfibrils by creating polyphosphoric acid aggregates, preliminarily constructing a 2–4 nm mesoporous framework while protecting the carbon hexagonal ring basic structure from excessive oxidation. During the KOH deep activation stage, a 3:1 KOH

solution reacts at 750 °C via $6KOH + C \rightarrow 2K + 3H_2 + 2K_2CO_3$. This reaction precisely etches micropores (primarily within the 0.5–1.2 nm range) onto the mesoporous framework pre-constructed by phosphoric acid, avoiding disordered pore expansion characteristic of homogeneous activation. The optimized impregnation ratio of 2:1–3:1 forms a self-consistent hierarchical system where the 2–4 nm mesopores function as rapid diffusion channels, allowing adsorbates quick access to adsorption sites. Meanwhile, the 0.5–1 nm micropores facilitate efficient adsorbate capture by leveraging their strong adsorption potential wells.

CO_2 adsorption performance

Adsorption isotherms

This study reveals the structure-performance relationship between CO_2 adsorption capacity and the evolution of micropore structure induced by H_3PO_4 activation in corn straw-based porous biochars, based on systematic pore structure characterization and gas adsorption model analysis. Figure 7 shows the static adsorption isotherms for CO_2 adsorption at 25 °C and 1 bar for different biochars. Langmuir model[34] as shown in Eq. (1), fitting results in Table 4 indicate that the maximum CO_2 adsorption capacity q_m initially increases, then decreases as the H_3PO_4 impregnation ratio increases. The capacity q_m reaches 3.43 mmol/g at a 3:1 ratio, while PKBC-4, which has a 54.4% mesopore proportion, plunges to 1.13 mmol/g. This nonlinear variation highly correlates with micropore volume data in Table 3. Among all samples, PKBC-3 exhibits the highest micropore volume (1.10 cm^3/g), whereas PKBC-4 suffers a 71% loss in micropore volume (0.32 cm^3/g) compared to PKBC-3. This loss directly leads to a 67% reduction in adsorption capacity. Notably, while PKBC-3 possesses optimal total pore volume (1.90 cm^3/g) and specific surface area (3,040 m^2/g), the increase in its adsorption capacity versus PKBC-2 (micropore volume 1.00 cm^3/g, adsorption capacity 3.34 mmol/g) is only 3%. This increase is significantly lower than the 10% rise in micropore volume. This implies that when the mesopore proportion exceeds a critical threshold of 42.1%, the synergistic effect of the pore structure begins to weaken.

$$q = \frac{q_m K_L P}{1 + K_L P} \quad (1)$$

where, q is the equilibrium adsorption capacity, mmol/g, q_m is the maximum monolayer adsorption capacity, mmol/g, K_L is the Langmuir adsorption equilibrium constant, /bar, and P is the pressure, bar.

Freundlich model[35] parameters, as shown in Eq. (2), support the proposed mechanism: all samples exhibit $1/n$ values close to 1 (1.05–1.18), indicating a relatively homogeneous surface energy distribution consistent with micropore-filling-dominated adsorption. However, PKBC-4 shows a contradictory combination of a usually high $1/n$ value (1.052) and a significantly lower K_F value [0.266 mmol/(g·bar$^{1/n}$)]. This discrepancy originates from heterogeneity in pore structure caused by excessive phosphoric acid, whereby residual phosphate ash selectively blocks 0.5–0.7 nm ultramicropores, forcing CO_2 molecules into weaker adsorption within wider mesopores (2–5 nm) or distorted micropores, manifesting as a cliff-like drop in the Freundlich constant K_F. This structural deterioration is more evident in Langmuir constant K_L variations: PKBC-3 achieves a K_L of 0.336 /bar, indicating a strong affinity for CO_2 molecules, while PKBC-4's K_L (0.093 /bar) falls below even the non-phosphoric acid-treated KBC sample (0.102 /bar). This confirms that excessive mesopore development weakens binding energy at adsorption sites. Moreover, the micropore volume exhibits near-perfect linear correlation with Langmuir adsorption capacity (R^2 = 0.998), whereas total pore volume correlation significantly deviates (R^2 = 0.703), establishing that micropores are the decisive factor for CO_2 adsorption capacity. The excellent fits of both Langmuir (homogeneous) and the Freundlich (heterogeneous) models reflect the dualistic pore structure of the biochar obtained in this study. Specifically, micropores provide uniform adsorption sites, while mesopores induce energetic heterogeneity.

Table 4 Isotherms parameters of different samples

Sample	Langmuir parameters			Freundich parameters		
	q_m (mmol/g)	K_L (/bar)	R^2	n	K_F (mmol/(g·bar$^{1/n}$))	R^2
KBC	1.4715	0.1018	0.9993	1.0568	0.4121	0.9976
PKBC-1	2.8623	0.1872	0.9998	1.1031	0.9314	0.9967
PKBC-2	3.3387	0.2677	0.9999	1.1448	1.5635	0.9936
PKBC-3	3.4341	0.3363	0.9929	1.1797	2.1513	0.9908
PKBC-4	1.1255	0.0929	0.9981	1.0523	0.2665	0.9927

$$q = K_F P^{1/n} \quad (2)$$

where, n is the heterogeneity index, K_F is the Freundlich adsorption capacity constant, mmol/(g·bar$^{1/n}$).

An analysis of adsorption efficiency per unit micropore volume reveals a paradoxical phenomenon: PKBC-2 achieves an absorption capacity of 3.27 mmol/cm^3, while PKBC-3 shows a slight decrease to 3.15 mmol/cm^3. In contrast, PKBC-4 exhibits an abnormal increase to 3.53 mmol/cm^3. This anomaly reveals the inherent contradiction in pore structure optimization. In PKBC-4, the blockage of large micropores (> 0.8 nm) forces CO_2 molecules into narrower pores (< 0.5 nm). As a result, although the adsorption density per unit pore volume increases, the absolute adsorption capacity collapses due to a drastically reduced effective adsorption volume. Conversely, PKBC-1 (mesopore proportion 27.2%) achieves an adsorption capacity of 4.4 mmol/g with a micropore volume of 0.65 cm^3/g, yielding a much higher unit micropore adsorption capacity (9.02 mmol/cm^3) compared to PKBC-2. This is attributed to a more concentrated micropore distribution in the 0.5–0.7 nm range. This size range creates superimposed potential wells that match the kinetic diameter of CO_2 molecules (0.33 nm), thereby enhancing the adsorption affinity[36]. This also explains why the PKBC-1's K_L (0.187 /bar) is 1.8 times greater than that of KBC (0.102 /bar).

This study integrated kinetic and thermodynamic parameters to establish a three-level regulation mechanism. The mechanism identifies that the micropore volume determines capacity, the micropore size tunes strength, and the mesopore proportion controls mass transfer. When the mesopore proportion is within the range

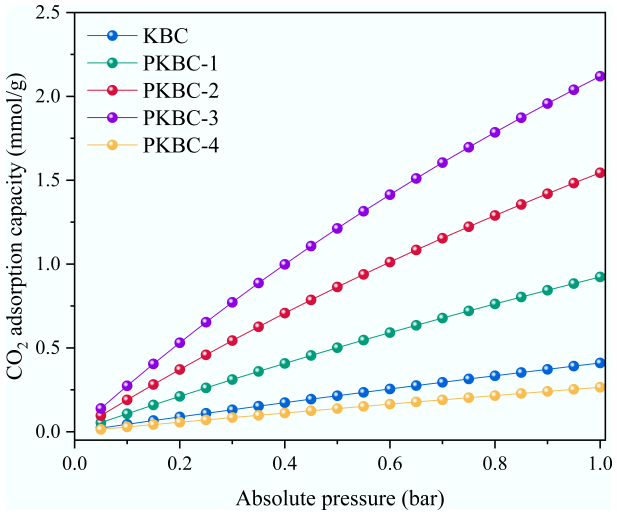

Fig. 7 CO_2 adsorption isotherms of different samples at 1 bar and 25 °C.

of 30%–40%, a well-developed mesopore network accelerates CO_2 transport to micropore active sites. However, exceeding the critical threshold of 42% for mesopore proportion disrupts the dynamic equilibrium between diffusion channels and adsorption sites. Although PKBC-4 has the largest mesopore volume (0.38 cm^3/g), its kinetic adsorption capacity is only 1.13 mmol/g due to insufficient density of micropore active site and deteriorated pore connectivity, confirming the adsorption dead zone effect. Therefore, an H_3PO_4 impregnation ratio between 2:1 and 3:1 achieves synergy between maximizing micropore volume and optimizing mesopore network, providing theoretical foundations and quantitative criteria for the targeted design of biomass-derived adsorbents.

Breakthrough curves

Fixed-bed breakthrough experiments reveals a significant nonlinear dependence between the dynamic CO_2 adsorption performance of corn straw-based porous biochar and the evolution of its mesoporous structure, as depicted in Fig. 8. At a H_3PO_4 impregnation ratio of 3:1, the breakthrough time t_b (when outlet concentration reached 10% of inlet concentration) peaked at 10.34 min, representing a 253% extension compared to KBC, which had the lowest mesopore proportion. Conversely, PKBC-4, with a 54.4% mesopore proportion, recorded a t_b of only 2.03 min. This phenomenon reveals the critical role of the mesoporous network, which demonstrates that as mesopore volume increased from 0.10 cm^3/g in KBC to 0.80 cm^3/g in PKBC-3, the length of the mass transfer zone on the breakthrough curve significantly shortened. This is reflected in the reduced difference between t_{90} (time when outlet concentration reached 90% of inlet concentration) and t_b, which decreased from 4.30 min for KBC to 4.10 min for PKBC-3. This confirms that mesoporous channels effectively accelerate the diffusion of CO_2 molecules towards the microporous active sites.

Notably, although PKBC-1 (27.2% mesopore proportion) possesses a moderate microporous volume (0.65 cm^3/g), its breakthrough curve displays an abnormally flat S-shape due to insufficient mesoporous volume (0.25 cm^3/g), resulting in a dynamic adsorption rate merely 58% of that for PKBC-3. The kinetic adsorption capacity q_{dyn} was calculated by real-time monitoring of outlet concentration changes using the material balance method[37] as shown in Eq. (3).

$$q_{dyn} = \frac{Q}{m}\int_0^{t_e}(C_{t0} - C_{tf})\mathrm{d}t \quad (3)$$

where, Q is the volumetric flow rate of CO_2, mL/min, m is the mass of adsorbent, g, C_{t0} is the concentration of CO_2 in the outlet gas at time t0, %, C_{tf} is the concentration of CO_2 in the outlet gas at time tf, %, t_e is the saturation time, min.

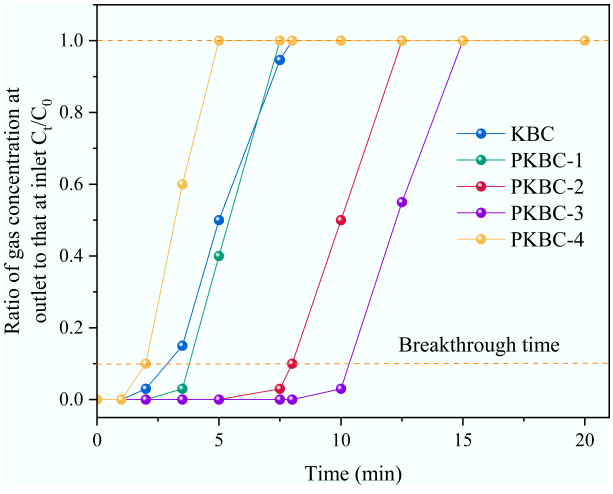

Fig. 8 The breakthrough curves of different samples at 25 °C.

The calculation results revealed that the q_{dyn} of PKBC-3 reached 3.02 mmol/g, approaching 88% of its Langmuir equilibrium adsorption capacity (3.43 mmol/g). In contrast, the mesopore-deficient KBC exhibited a much lower q_{dyn} of only 1.18 mmol/g (80% of equilibrium capacity). This disparity can be attributed to the regulation of mass transfer efficiency by mesopores. When the mesopore proportion declined to below 30%, the diffusion of CO_2 molecules through tortuous micropores was hindered, resulting in the dynamic adsorption capacity that was considerably lower than the theoretical equilibrium value. When the mesopore proportion increased to approximately 40%, the well-developed mesoporous network facilitated rapid access for gas molecules to deep micropores, elevating the q_{dyn}/q_m ratio to 85%. A detailed analysis of breakthrough curve morphology demonstrated that the mesopore proportion influenced dynamic adsorption through dual mechanisms. First, a positive correlation was observed between mesopore volume and the average adsorption rate (q_{dyn}/t_e) (R^2 = 0.967). PKBC-3 reached an average adsorption rate of 0.5345 mmol/(g·min), which exceeded that of KBC [0.4975 mmol/(g·min)]. Second, an optimal range existed for the relationship between mesopore proportion and breakthrough curve steepness [defined as $(t_{90} - t_b)/t_b$]. PKBC-2 and PKBC-3 exhibited values of 0.50 and 0.45, respectively, while KBC showed a high value of 1.47. This steepness effect reversed in PKBC-4. Despite possessing the highest mesopore proportion (54.4%), the collapse of microporous volume (0.32 cm^3/g) resulted in a small tb-t_{90} difference (2.59 min). This indicates inefficient mass transfer and rapid breakthrough due to a severe insufficiency of adsorption sites. Its q_{dyn} was only 1.03 mmol/g (91.3% of equilibrium capacity), confirming that rapid mass transfer without sufficient adsorption sites is not practically valuable. By integrating static and dynamic adsorption data, the mesoporous structure exhibited a bidirectional regulation mechanism. When the mesopore proportion was below 35%, limited diffusion channels caused adsorption kinetics to become the performance bottleneck, resulting in flat breakthrough curves and low t_b values. Conversely, when the mesopore proportion exceeded 50%, the loss of microporous active sites shifted adsorption capacity to the dominant limiting factor, as faster mass transfer could not compensate for the reduced adsorption capacity. Within the narrow window around 40% mesopore proportion, the material concurrently achieved both maximum adsorption capacity (3.43 mmol/g) and optimal mass transfer efficiency (t_b = 10.34 min), resulting in breakthrough curves characterized by a steep front and a long plateau. This finding offers a key design criterion for biomass-based CO_2 adsorbents in engineering applications. Precisely constructing hierarchical pore structures with approximately 40% mesopore proportion by regulating the H_3PO_4 impregnation ratio can synergistically overcome the traditional trade-off constraints between adsorption capacity and kinetic rate.

Adsorption kinetics

Figure 9 presents the CO_2 adsorption kinetic curves for various samples at 25 °C. The analysis utilized the Pseudo-first order, Pseudo-second order, and Avrami models as shown in Eq. (4)–Eq. (6)[38–40], with the fitting results summarized in Tables 5–7. Quasi-equilibrium kinetic studies revealed the regulatory mechanism of mesoporous structure on CO_2 diffusion energy barriers and its structure-activity relationship with the adsorption rate. Avrami model fitting indicated that PKBC-3 had an adsorption rate constant k_A of 0.491 /min, representing a 180% increase compared to mesopore-deficient KBC (0.175 /min). The enhancement observed is directly related to PKBC-3, which has the highest mesopore volume (0.80 cm^3/g) and a mesopore proportion (42.1%) among all samples. Notably, apparent activation energies derived from the Arrhenius equation reveal a significant trend. PKBC-3

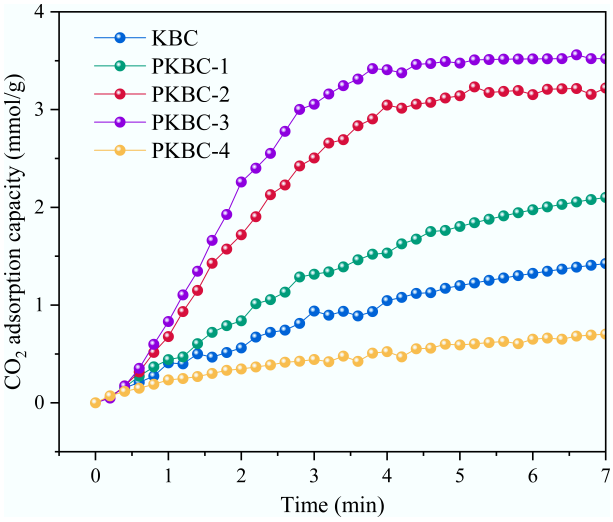

Fig. 9 Adsorption kinetics curves for CO_2 adsorption of different samples at 25 °C.

displayed a low activation energy of 8.29 kJ/mol, while KBC, with only 27.2% mesopore proportion, reached 18.73 kJ/mol. This energy difference originated from the mass transfer bridge function of the mesoporous network. As the mesopore volume increased from 0.10 cm^3/g in KBC to 0.80 cm^3/g in PKBC-3, the diffusion path energy barrier for CO_2 molecules traveling toward microporous active sites was substantially reduced. Consequently, the adsorption half-life of PKBC-3 at 298 K shortened to 1.41 min, which is merely 36% of that for KBC (3.95 min). The evolution of kinetic model applicability further corroborated this mechanism. When the mesopore proportion was below 30% (KBC and PKBC-1), the superiority of the pseudo-first-order model (R^2 > 0.99) indicated that adsorption was controlled by single-phase diffusion. The high activation energies (18.73 kJ/mol for KBC, 15.54 kJ/mol for PKBC-1) reflected strong diffusion resistance caused by tortuous micropore pathways. In contrast, when mesopore proportion rose to approximately 40% (PKBC-2 and PKBC-3), the Avrami model showed an optimal fit (R^2 > 0.99) with parameter value n increasing to 1.66–1.84, confirming the adsorption process into a cooperative mechanism involving rapid mesopore diffusion and micropore filling. Correspondingly, the activation energy decreased below 10 kJ/mol (9.77 kJ/mol for PKBC-2, 8.29 kJ/mol for PKBC-3). Notably, although PKBC-4 possessed the highest mesopore proportion (54.4%), its activation energy rebounded to 14.67 kJ/mol due to the collapsed microporous structure (V_{micro} = 0.32 cm^3/g). Residual phosphate-induced pore blockage forced CO_2 molecules to navigate disordered mesopore labyrinths, paradoxically increasing the diffusion energy barrier[41].

$$q = q_e(1 - e^{-k_1 t}) \quad (4)$$

$$q = \frac{k_2 q_e^2 t}{1 + k_2 q_e t} \quad (5)$$

$$q = q_e(1 - e^{-(k_A t)^n}) \quad (6)$$

where, q_e is the theoretical equilibrium adsorption capacity, mmol/g, k_1 is the Pseudo-first-order rate constant, 1/min, k_2 is the Pseudo-second-order rate constant, g/(mmol·min), k_A is the Avrami rate constant, 1/min, n is the Avrami index.

The correlation analysis of static and dynamic adsorption data confirmed the central role of mesopores. The average adsorption rate of PKBC-3 in breakthrough experiments [0.776 mmol/(g·min)] was 5.7 times higher than that of KBC [0.136 mmol/(g·min)]. This finding aligns closely with their activation energy difference (ΔE_a = 10.44 kJ/mol). According to transition state theory, a 10 kJ/mol reduction in activation energy can increase reaction rates by approximately 50-fold at 298 K. Particularly, under quasi-equilibrium kinetics at 25 °C, PKBC-3 reached 90% of its equilibrium adsorption capacity in just 4.7 min, while Group A required 12.3 min, proving that materials with lower activation energy can better utilize thermal energy to overcome diffusion resistance. By integrating V_{meso}, activation energy (E_a), and Avrami rate constant (k_A), a mesopore proportion threshold of approximately 40% minimized the diffusion energy barrier. When the mesopore proportion was below 30%, E_a decreased linearly with increasing mesopores. When the mesopore proportion exceeded 50%, adsorption site scarcity due to the loss of micropore paradoxically elevated the effective diffusion barrier (E_a for PKBC-4 was 77% higher than PKBC-3). Only within the optimal mesopore proportion range around 40% could the material achieve both maximum microporous volume (1.10 cm^3/g) and minimum activation energy (8.29 kJ/mol). This synergy enabled CO_2 adsorption with both high capacity and rapid kinetics, providing quantitative theoretical support for energy barrier engineering design in biomass-based adsorbents.

Table 5 Kinetic parameters of CO_2 adsorption of different samples fitted by Pseudo-first order model

Sample	q_e (mmol/g)	k_1 (1/min)	R^2
KBC	1.6615	0.1904	0.9946
PKBC-1	2.1262	0.1837	0.9957
PKBC-2	4.2337	0.3188	0.9709
PKBC-3	4.6811	0.3901	0.9581
PKBC-4	1.1883	0.2812	0.9809

Table 6 Kinetic parameters of CO_2 adsorption of different samples fitted by Pseudo-second order model

Sample	q_e (mmol/g)	k_2 [g/(mmol·min)]	R^2
KBC	5.3659	0.0172	0.9945
PKBC-1	8.5141	0.0102	0.9946
PKBC-2	11.6545	0.0169	0.9620
PKBC-3	11.7385	0.0219	0.9440
PKBC-4	1.7005	0.0811	0.9856

Table 7 Kinetic parameters of CO_2 adsorption of different samples fitted by Avrami model

Sample	q_e (mmol/g)	k_A (1/min)	n	R^2
KBC	2.1881	0.1755	0.9725	0.9946
PKBC-1	2.6693	0.2713	1.2194	0.9986
PKBC-2	3.7394	0.4331	1.6640	0.9991
PKBC-3	4.4478	0.4912	1.8423	0.9995
PKBC-4	1.6798	0.0426	0.6701	0.9909

CO_2 adsorption mechanism

To contextualize the properties of PKBC-3, it was benchmarked against recent high-performance biochars from representative studies, as shown in Table 8. The specific surface area of PKBC-3 significantly surpasses that of other biochars, and its CO_2 adsorption capacity is also highly competitive. This performance is a result of the unique microwave-assisted H_3PO_4/KOH dual activation, which synergistically maximizes micropore volume while maintaining optimal mesopore connectivity.

Table 8 SSAs and CO_2 adsorption capacities of biochars

Feedstocks	Conditions	SSA (m^2/g)	Adsorption capacity (mmol/g)	Ref.
Corn straw	KOH : biochar = 2:1, tube furnace, 700 °C, 60 min	1,631.77	3.06 at 25 °C	[42]
Corn straw	KOH : biochar = 0.1:1, biomass gasifier, 450 °C, 120 min	365.11	2.88	[43]
Corn straw	TEPA, muffle furnace, 700 °C, 120 min	423	2.38 at 60 °C	[44]
Pine	KOH : biochar = 2:1, tube furnace, 800 °C, 60 min	1,709.04	3.79 at 25 °C	[42]
Sugarcane bagasse	TEPA, muffle furnace, 700 °C, 120 min	352	2.22 at 60 °C	[44]
Miscanthus	TEPA, muffle furnace, 700 °C, 120 min	532	2.89 at 60 °C	[44]
Switchgrass	TEPA, muffle furnace, 700 °C, 120 min	520	2.51 at 60 °C	[44]
Rambutan peel	Tube furnace, 900 °C, 90 min	569.64	1.56 at 30 °C	[45]
Rice husk	KOH : biochar = 1:1, 750 °C	1439	3.51 at 25 °C	[46]
Blue algal	KOH : biochar = 0.5:1, tube furnace, 800 °C, 120 min	1,018.55	2.76 at 25 °C	[47]
Poplar wood chip	$K_2C_2O_4$, 800 °C, 120 min	1,418	3.82 at 25 °C	[48]
Corn straw	H_3PO_4 + KOH, 750 °C, 60 min	3,038.92	3.43 at 25 °C	This study

The pore structures and adsorption performance data from five corn straw-based biochars uncovered a bidirectional regulatory mechanism of the mesopore proportion ratio (V_{meso}/V_{total}) and its impact on CO_2 adsorption capacity and kinetics. Figure 10 illustrates the maximum adsorption capacity, average adsorption rate, and activation energy for CO_2 adsorption across different biochars. When the mesopore proportion ratio falls below 30%, the materials retain a high micropore volume (0.50–0.65 cm^3/g) and adsorption capacity. However, their restricted mesopore network (V_{meso} = 0.10–0.25 cm^3/g) results in convoluted diffusion pathways for CO_2 molecules trying to access micropore sites. This manifests as high activation energy (15.54–18.73 kJ/mol) and low average adsorption rate [0.50–0.51 mmol/(g·min)]. At this stage, mass transfer resistance becomes the primary obstacle to adsorption kinetics, which has been evidenced by a significantly prolonged $t_{90} - t_b$ value of 4.30 min for KBC in breakthrough curves, confirming that CO_2 migration within the micropores must overcome multiple energy barriers.

As the mesopore proportion ratio increases to about 40%, well-developed mesopore channels (V_{meso} = 0.64–0.80 cm^3/g) substantially optimize mass transfer pathways. First, mesopores function as high-speed diffusion channels, reducing the average distance for CO_2 molecules to reach micropore active sites, which decreases the diffusion activation energy to below 10 kJ/mol. Second, the continuous network structure enhances connectivity between micropores, preventing the formation of adsorption dead zones. This synergy elevates the average adsorption rate of PKBC-3 to 0.53 mmol/(g·min), while the micropore volume peaks at 1.10 cm^3/g, resulting in a maximum equilibrium adsorption capacity (3.43 mmol/g).

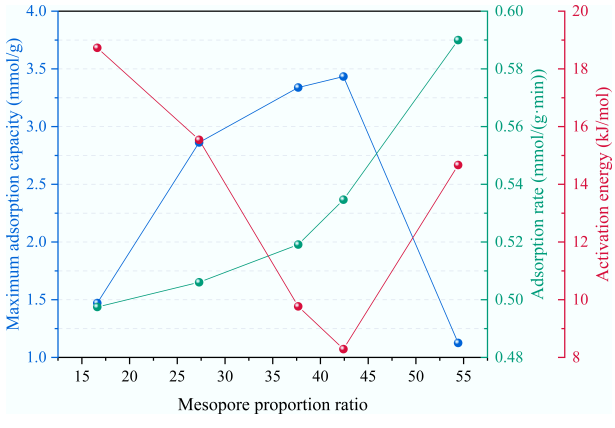

Fig. 10 The maximum adsorption capacity, average adsorption rate, and activation energy for CO_2 adsorption of different samples.

When the proportion of mesopores exceeds 50%, an excessive amount of H_3PO_4 causes pore structure imbalance. The micropore volume plummets to 0.32 cm^3/g, and residual phosphates partially block pore channels, creating disordered mesopore labyrinths. Although the mesopore volume (0.38 cm^3/g) still provides low diffusion resistance [activation energy 14.67 kJ/mol, adsorption rate 0.59 mmol/(g·min)], the severe reduction in micropore active sites causes a sharp decline in adsorption capacity to 1.13 mmol/g. Under these conditions, the breakthrough curve exhibits a sudden increase but a rapid saturation profile (t_b merely 2.03 min), indicating that CO_2 molecules rapidly traverse mesopores but remain uncaptured due to insufficient adsorption sites. This phenomenon highlights that rapid mass transfer without effective adsorption sites holds no practical value[49].

Conclusions

This study proposes a microwave-assisted two-step activation (preliminary H_3PO_4 activation and KOH etching) strategy for synthesizing hierarchically porous biochar from corn straw, aimed at efficiently capturing CO_2. The influence of the H_3PO_4-to-biomass impregnation ratio on biochar performance was investigated. The main contributions are as follows. (1) Methodological innovation. An H_3PO_4/KOH two-step activation protocol synergizing with microwave pyrolysis was developed, enabling precise control over mesopore proportion via H_3PO_4 impregnation ratio modulation. As the H_3PO_4 impregnation ratio increased from 1:1 to 3:1, the specific surface area, micropore volume, and mesopore volume proportion of the resulting biochar increased from 2,088.10 m^2/g, 0.653 cm^3/g, and 27.28% to 3,038.92 m^2/g, 1.089 cm^3/g, and 42.41%, respectively. Excessive phosphoric acid substantially increased the mesopore proportion while reducing both the specific surface area and micropore volume. (2) Scientific discovery. A mesopore proportion threshold of ≈40% (PKBC -3 with 42.4%) was identified, which optimally balances CO_2 adsorption capacity and kinetic dynamic capacity. This resolves the long-standing trade-off between micropore-dominated capacity and mesopore-dominated mass transfer. The CO_2 adsorption results indicate that biochar PKBC-3 prepared with an H_3PO_4 impregnation ratio of 3:1 exhibited optimal adsorption performance, achieving a maximum CO_2 adsorption capacity of 3.434 mmol/g at 25 °C and 1 bar. Its dynamic adsorption capacity reached 3.02 mmol/g under 15% CO_2 at 100 mL/min. Mechanistically, mesopores play a crucial role as diffusion channels, reducing barriers for CO_2 migration to micropore sites. With a mesopore proportion below 30%, micropore pathways become predominantly tortuous, increasing activation energy and restricting adsorption kinetics. Conversely, if the mesopore proportion exceeds 50%, the excess H_3PO_4 can lead to micropore collapse and phosphate

blockage. Although residual mesopores enhance diffusion, this irreversibly sacrifices capacity. This work establishes mesopore proportion as a central design parameter for CO_2 adsorbents. Future work should focus on scaling up the two-step activation process for industrial flue gas treatment and implementing surface functionalization to further improve CO_2 selectivity.

Author contributions

The authors confirm contributions to the paper as follows: study conception: Qiu T, Mostafa E, Zhang Y; data collection: Qiu T, Cao W, Xie K, Ahmad F; analysis and interpretation of results: Qiu T, Zhao W; draft manuscript preparation: Qiu T, Zhang Y. All authors reviewed the results and approved the final version of the manuscript.

Data availability

The datasets used or analyzed during the current study are available from the corresponding author upon reasonable requests.

Funding

This work was supported by the National Natural Science Foundation of China (Grant No. 52476005), and Heilongjiang Provincial Key R&D Program 'Unveiling the Leader' Project (Grant No. 2023ZXJ02C04).

Declarations

Competing interests

The authors declare that they have no conflict of interest.

Author details

[1]School of Energy Science and Engineering, Harbin Institute of Technology, Harbin 150001, China; [2]Faculty of Agriculture, Cairo University, Giza 12613, Egypt

References

[1] Jeewani PH, Brown RW, Rhymes JM, Mcnamara NP, Chadwick DR, et al. 2025. Greenhouse gas removal in agricultural peatland via raised water levels and soil amendment. *Biochar* 7(1):39

[2] Desjardins SM, Ter-Mikaelian MT, Chen J. 2024. Cradle-to-gate life cycle analysis of slow pyrolysis biochar from forest harvest residues in Ontario, Canada. *Biochar* 6(1):58

[3] Mehta D. 2024. Towards carbon neutrality: asymmetric impact of financial development and digitalization on carbon dioxide emissions in Mediterranean countries. *Carbon Research* 3:76

[4] Matenda FR, Raihan A, Zhou H, Sibanda M. 2024. The influence of economic growth, fossil and renewable energy, technological innovation, and globalisation on carbon dioxide emissions in South Africa. *Carbon Research* 3:69

[5] Nwaoha C, Odoh K, Ikpatt E, Orji R, Idem R. 2017. Process simulation, parametric sensitivity analysis and ANFIS modeling of CO_2 capture from natural gas using aqueous MDEA–PZ blend solution. *Journal of Environmental Chemical Engineering* 5(6):5588–5598

[6] Zhan L, Lu W, Xiang Q, Chen Z, Luo W, et al. 2025. Construction of low-energy regenerative bagasse-based carbon capture material for high efficiency CO_2 capture. *Journal of Colloid and Interface Science* 687:261–270

[7] Lee Y, Kim YT, Kwon EE, Lee J. 2020. Biochar as a catalytic material for the production of 1,4-butanediol and tetrahydrofuran from furan. *Environmental Research* 184:109325

[8] Bolan N, Hoang SA, Beiyuan J, Gupta S, Hou D, et al. 2022. Multifunctional applications of biochar beyond carbon storage. *International Materials Reviews* 67(2):150–200

[9] Ma J, Li L, Wang H, Du Y, Ma J, et al. 2022. Carbon capture and storage: history and the road ahead. *Engineering* 14:33–43

[10] Dissanayake PD, You S, Igalavithana AD, Xia Y, Bhatnagar A, et al. 2020. Biochar-based adsorbents for carbon dioxide capture: a critical review. *Renewable and Sustainable Energy Reviews* 119:109582

[11] Zhang G, Zhang L, Shi Z, Yang Y, Liu J. 2025. Microbial nutrient limitation and carbon use efficiency in saline-alkali soil amended with biochar: insights from ecoenzymatic C : N : P stoichiometry. *Biochar* 7(1):68

[12] Ngaba MJY, Yemele OM, Hu B, Rennenberg H. 2025. Biochar application as a green clean-up method: bibliometric analysis of current trends and future perspectives. *Biochar* 7(1):83

[13] Wu C, Wang Y, Clarke JL, Su H, Wang L, et al. 2025. Biochar enhances the sorption and degradation of fluridone and its main metabolite in soil: insights into biodegradation potential and remediation of microbial communities. *Biochar* 7(1):81

[14] Salinas-Farran L, Mosonik MC, Jervis R, Marathe S, Rau C, et al. 2024. Tracked evolution of single biochar particle's morphology during pyrolysis in operando X-ray micro-computed tomography. *Biochar* 6(1):86

[15] Yu Q, Zhang X, Gao T, Gong X, Wu J, et al. 2024. Converting plastic-contaminated agricultural residues into fit-for-purpose biochar soil amendment: an initial study. *Biochar* 6(1):98

[16] Wang T, Liu H, Toan S, Sun Z, Sun Z. 2024. Deoxygenated pyrolysis-gasification of biomass for intensified bio-oil and syngas co-production with tar abatement. *Fuel* 371:131883

[17] Chowdhury P, Chowdhury T, Chowdhury H, Bontempi E. 2025. Food waste to biochar; a potential sustainable solution for Australia: a comprehensive review. *Carbon Research* 4:41

[18] Qiao Y, Wu C. 2022. Nitrogen enriched biochar used as CO_2 adsorbents: a brief review. *Carbon Capture Science & Technology* 2:100018

[19] Zhang Y, Chen P, Liu S, Peng P, Min M, et al. 2017. Effects of feedstock characteristics on microwave-assisted pyrolysis–a review. *Bioresource Technology* 230:143–151

[20] Qiu T, Liu C, Cui L, Liu H, Muhammad K, et al. 2023. Comparison of corn straw biochars from electrical pyrolysis and microwave pyrolysis. *Energy Sources Part A: Recovery Utilization and Environmental Effects* 45(1):636–649

[21] Huang YF, Chiueh PT, Shih CH, Lo SL, Sun L, et al. 2015. Microwave pyrolysis of rice straw to produce biochar as an adsorbent for CO_2 capture. *Energy* 84:75–82

[22] Premchand P, Demichelis F, Galletti C, Chiaramonti D, Bensaid S, et al. 2024. Enhancing biochar production: a technical analysis of the combined influence of chemical activation (KOH and NaOH) and pyrolysis atmospheres (N_2/CO_2) on yields and properties of rice husk-derived biochar. *Journal of Environmental Management* 370:123034

[23] Li D, Sun L, He R, Xiao G, Zhu D, et al. 2024. Hierarchically porous MgO/biochar composites for efficient CO_2 capture: structure, performance and mechanism. *Chemical Engineering Journal* 498:155607

[24] Zhang J, Zhang X, Li X, Song Z, Shao J, et al. 2024. Prediction of CO_2 adsorption of biochar under KOH activation via machine learning. *Carbon Capture Science & Technology* 13:100309

[25] Guo T, Zhang Y, Geng Y, Chen J, Zhu Z, et al. 2023. Surface oxidation modification of nitrogen doping biochar for enhancing CO_2 adsorption. *Industrial Crops and Products* 206:117582

[26] Xie WH, Yao X, Li H, Li HR, He LN. 2022. Biomass-based N-rich porous carbon materials for CO_2 capture and in-situ conversion. *ChemSusChem* 15(18):e202201004

[27] Mestre AS, Pires J, Nogueira JMF, Parra JB, Carvalho AP, et al. 2009. Waste-derived activated carbons for removal of ibuprofen from solution: role of surface chemistry and pore structure. *Bioresource Technology* 100(5):1720–1726

[28] Pang B, Zheng H, Jin Z, Hou D, Zhang Y, et al. 2024. Inner superhydrophobic materials based on waste fly ash: microstructural morphology of microetching effects. *Composites Part B: Engineering* 268:111089

[29] Zhang J, Shao J, Jin Q, Zhang X, Yang H, et al. 2020. Effect of deashing on activation process and lead adsorption capacities of sludge-based biochar. *Science of the Total Environment* 716:137016

[30] Rehman A, Heo YJ, Nazir G, Park SJ. 2021. Solvent-free, one-pot synthesis of nitrogen-tailored alkali-activated microporous carbons with an efficient CO_2 adsorption. *Carbon* 172:71–82

[31] Potnuri R, Surya DV, Rao CS, Yadav A, Sridevi V, et al. 2023. A review on analysis of biochar produced from microwave-assisted pyrolysis of agricultural waste biomass. *Journal of Analytical and Applied Pyrolysis* 173:106094

[32] Shoaib AGM, Yılmaz M, El Sikaily A, Hassaan MA, El-Nemr MA, et al. 2025. Isotherm, kinetics and ANN analysis of methylene blue adsorption onto nitrogen doped *Ulva lactuca* Biochar. *Scientific Reports* 15(1):10642

[33] Chen Y, Zhou C, Xing X, Chen L, Yao B, et al. 2024. Interconnected pyrolysis and activation with in-situ H_3PO_4 activation of biochar from pear wood chips in a pilot scale dual fluidized bed. *Chemical Engineering Journal* 495:153579

[34] Huang Q, Karthik H, Patra BR, Pattnaik F, Dalai AK. 2025. Preparation of an adsorbent derived from canola hull by slow pyrolysis for effective carbon dioxide adsorption. *Canadian Journal of Chemistry* 103(6):293–306

[35] Oginni O, Singh K, Oporto G, Dawson-Andoh B, McDonald L, et al. 2019. Influence of one-step and two-step KOH activation on activated carbon characteristics. *Bioresource Technology Reports* 7:100266

[36] Khandaker T, Hossain MS, Dhar PK, Rahman MS, Hossain MA, et al. 2020. Efficacies of carbon-based adsorbents for carbon dioxide capture. *Processes* 8(6):654

[37] Liang W, Ma C, Zhu Y, Liu J. 2025. Performance and mechanism of modified red mud for the toluene adsorption. *Journal of Environmental Chemical Engineering* 13(2):115587

[38] Liang W, Zhang Y, Yang L, Liu J. 2025. Adsorption performance of amine-functionalized red mud-based adsorbent for CO_2 capture. *Journal of Environmental Management* 383:125334

[39] Zuhara S, McKay G. 2025. Single and binary pollutant adsorption of strontium and barium on waste-derived activated carbons: modelling, regeneration and mechanistic insights. *Environmental Technology & Innovation* 39:104220

[40] Lo CY, Hanh NTD, Srinophakun P, Prapainainar P, Chiu CY, et al. 2025. Development and characterization of dual functional weak-strong acidic ion exchange nanofiber membranes for efficient lysozyme adsorption in batch mode. *Food Chemistry* 487:144750

[41] He N, Hu D, Xie H, Wu Z, Wang Z, et al. 2025. Sustainable production of sawdust-derived porous carbon: distinguished roles of phosphates and polyphosphates on pore evolution and tetracycline hydrochloride purification. *Separation and Purification Technology* 363(1):132101

[42] Zhang T, Xiong Z, Zhao Y, Zhang J. 2025. Comparative study on the adsorption performance of CO_2 and Hg in flue gas using corn straw and pine biochar modified by KOH. *Separation and Purification Technology* 359(2):130757

[43] Wang H, Wang X, Teng H, Xu J, Sheng L. 2022. Purification mechanism of city tail water by constructed wetland substrate with NaOH-modified corn straw biochar. *Ecotoxicology and Environmental Safety* 238:113597

[44] Chatterjee R, Sajjadi B, Chen WY, Mattern DL, Hammer N, et al. 2020. Effect of pyrolysis temperature on PhysicoChemical properties and acoustic-based amination of biochar for efficient CO_2 adsorption. *Frontiers in Energy Research* 8:85

[45] Zubbri NA, Mohamed AR, Kamiuchi N, Mohammadi M. 2020. Enhancement of CO_2 adsorption on biochar sorbent modified by metal incorporation. *Environmental Science and Pollution Research* 27(11):11809–11829

[46] Wang S, Lee YR, Won Y, Kim H, Jeong SE, et al. 2022. Development of high-performance adsorbent using KOH-impregnated rice husk-based activated carbon for indoor CO_2 adsorption. *Chemical Engineering Journal* 437(1):135378

[47] Wang H, Wang H, Liu G, Yan Q. 2021. In-situ pyrolysis of Taihu blue algae biomass as appealing porous carbon adsorbent for CO_2 capture: role of the intrinsic N. *Science of The Total Environment* 771:145424

[48] Guo X, Zhang G, Wu C, Liu J, Li G, et al. 2021. A cost-effective synthesis of heteroatom-doped porous carbon by sulfur-containing waste liquid treatment: as a promising adsorbent for CO_2 capture. *Journal of Environmental Chemical Engineering* 9(1):105165

[49] Hsu CJ, Kuo IL, Hsi HC, Lam SS, Huang YP, et al. 2025. Single-step pyrolytic synthesis of ultra-microporous ammonialized biochar for carbon dioxide capture. *Journal of Environmental Management* 381:125197